INTERNATIONAL JOURNAL FOR NUMERICAL METHODS IN FLUIDS, VOL. 17, 1035–1054 (1993)

A HEIGHT–FLUX METHOD FOR SIMULATING FREE SURFACE FLOWS AND INTERFACES

F. MASHAYEK AND N. ASHGRIZ

Department of Mechanical and Aerospace Engineering, Clifford C. Furnas Hall, State University of New York at Buffalo, Buffalo, NY 14260, U.S.A.

SUMMARY

A new technique for the numerical simulation of the free surface flows is developed. This technique is based on the finite element method with penalty formulation, and a flux method for surface advection. The advection part which is completely independent of the momentum solver is based on subdividing the fluid domain into small subvolumes along one of the co-ordinate axis. The subvolumes are then used to find the height function which will later describe the free surface. The free surface of the fluid in each subvolume is approximated by a line segment and its slope is calculated using the volume of the fluid in the two neighbouring subvolumes. Later, the unidirectional volume flux from one subvolume to its neighbouring one is calculated using the conservation laws, and the new surface line segments are reconstructed. This technique, referred to as the Height–Flux Method (HFM) is implemented to simulate the temporal instability of a capillary jet. The results of the numerical simulation well predict the experimental data. It is also shown that the HFM is computationally more efficient than the techniques which use a kinematic boundary condition for the surface advection.

KEY WORDS Free surface flows Interfaces Volume of fluid Liquid jet

1. INTRODUCTION

In the numerical simulation of viscous fluid flows with free surfaces and interfaces, a technique has to be devised to track the motion of these surfaces. Depending on the complexity of the surface/interface topology, different techniques are preferred. For very complicated surface motion with surface merging and surface breaking, Marker And Cell (MAC) and Volume Of Fluid (VOF) methods are normally used.[1–6] Finite element methods are preferred in problems with less complicated surface deformations.[7–12] The conventional Galerkin method on a fixed mesh and purely Lagrangian approach where nodes are fluid particles are common techniques to track the surface in such cases.

The Lagrangian method seems natural in tracking the free surface or the interface. However, it may result in overdistorted grids, and therefore may require somewhat intricate remeshing procedures. In this technique the unknown fields are interpolated by finite element basis functions defined on a continuously deforming grid. The displacement of the free surface is unknown *a priori* and is determined simultaneously with the unknown fields. Then, at each discrete time step, the grid is deformed to follow the motion of the free surface in a way that avoids excessive element deformations and the unknown field is calculated again.

Another more common technique is the height method,[13,14] which is a particular case of the method of spines by Kistler and Scriven.[15] In a two-dimensional problem, the free surface is

0271–2091/93/241035–20$15.00

Received 1 March 1993
Revised 8 June 1993

represented by a function of time and a single space co-ordinate, i.e. height function. The evolution of the free surface is then determined by the kinematic condition for the surface. Here, the motion of the internal nodes is related to the displacement of the free surface or interface.

In this paper a new technique for tracking of the free surfaces, which utilizes the conservation of mass rather than the kinematic condition, is presented. In Section 2 the generalized governing equations for the simulation of the free surface flows are given, followed by their finite element formulation in Section 3. The surface advection technique is described in Section 4 and it is applied to the capillary jet instability problem in Section 5. The concluding remarks are given in Section 6.

2. GOVERNING EQUATIONS

Consider the laminar flow of an incompressible and viscous fluid with a free surface. Assuming constant properties for the fluid, the governing equations of the flow in non-dimensional form are

$$\frac{\partial u}{\partial z}+\frac{1}{r^\beta}\frac{\partial}{\partial r}(r^\beta v)=0, \tag{1}$$

$$\frac{\partial u}{\partial t}+u\frac{\partial u}{\partial z}+v\frac{\partial u}{\partial r}=-\frac{\partial p}{\partial z}+\frac{1}{Re}\left[\frac{\partial^2 u}{\partial z^2}+\frac{1}{r^\beta}\frac{\partial}{\partial r}\left(r^\beta\frac{\partial u}{\partial r}\right)\right], \tag{2}$$

$$\frac{\partial v}{\partial t}+u\frac{\partial v}{\partial z}+v\frac{\partial v}{\partial r}=-\frac{\partial p}{\partial r}+\frac{1}{Re}\left[\frac{\partial^2 v}{\partial z^2}+\frac{1}{r^\beta}\frac{\partial}{\partial r}\left(r^\beta\frac{\partial v}{\partial r}\right)-\beta\frac{v}{r^2}\right], \tag{3}$$

where $\beta=0$ for 2D Cartesian and $\beta=1$ for axisymmetric flows. The non-dimensional parameters have been defined as

$$z=\frac{z'}{L},\qquad r=\frac{r'}{L},\qquad t=\frac{t'U}{L},$$

$$u=\frac{u'}{U},\qquad v=\frac{v'}{U},\qquad p=\frac{p'}{\rho U^2},$$

$$Re=\frac{\rho UL}{\mu},\qquad We=\frac{\rho U^2 L}{\sigma},$$

with L and U being the characteristic scales of length and velocity, respectively. The density, viscosity, and surface tension of the fluid are represented by ρ, μ and σ.

The boundary conditions are given by

$$\begin{cases} u=F(z,r) \\ v=G(z,r) \end{cases} \quad \text{on } S_1, \tag{4}$$

$$\begin{aligned} \bar{\tau}_{zz}&=\frac{\bar{\tau}'_{z'z'}}{\rho U^2}=\left(\frac{2}{Re}\frac{\partial u}{\partial z}-p\right)n_z+\frac{1}{Re}\left(\frac{\partial u}{\partial r}+\frac{\partial v}{\partial z}\right)n_r \\ \bar{\tau}_{rr}&=\frac{\bar{\tau}'_{r'r'}}{\rho U^2}=\frac{1}{Re}\left(\frac{\partial u}{\partial r}+\frac{\partial v}{\partial z}\right)n_z+\left(\frac{2}{Re}\frac{\partial v}{\partial r}-p\right)n_r \end{aligned} \quad \text{on } S_2, \tag{5}$$

where S_1 and S_2 are parts of the boundary with Dirichlet and Neumann boundary conditions, respectively. $\bar{\tau}_{zz}$ and $\bar{\tau}_{rr}$ denote z and r components of the total surface traction and n_z and n_r denote direction cosines of the unit outer normal to the surface S_2. On the free surface, $\bar{\tau}_{zz}$ and $\bar{\tau}_{rr}$

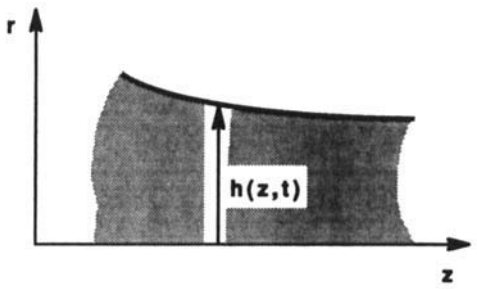

Figure 1. An axisymmetric fluid domain represented by a height function

are the components of the surface tension which are inversely proportional to the radius of curvature of the surface R'_c. Therefore,

$$\bar{\tau}_{zz}=\frac{\sigma/R'_c}{\rho U^2}n_z=\frac{1}{We}\frac{1}{R_c}n_z,$$
$$\bar{\tau}_{rr}=\frac{\sigma/R'_c}{\rho U^2}n_r=\frac{1}{We}\frac{1}{R_c}n_r. \tag{6}$$

The non-dimensionalised radius of curvature of an axisymmetric surface is

$$\frac{1}{R_c}=\frac{1}{R_1}+\frac{1}{R_2},$$

with R_1 and R_2* being the principal radii of curvature of the surface. We assume that the free surface can be represented by a height function $h(z, t)$, which is independent of the radius r, as shown in Figure 1. Therefore, R_1 and R_2 are given by

$$R_1=\frac{[1+(\partial h/\partial z)^2]^{1\cdot5}}{\partial^2 h/\partial z^2},$$
$$R_2=-h\left[1+\left(\frac{\partial h}{\partial z}\right)^2\right]^{0\cdot5}.$$

In the problems considered in this paper there is no contact between the free surface and solid walls; therefore, the contact angles are not modelled here.

3. FINITE ELEMENT FORMULATION

We use the Galerkin finite element method to solve equations (1)–(3). In accordance with the advection method described in Section 4, the solution should be in terms of the primitive variables and, due to the significance of the surface tension effects in free surface flows, it has to be capable of handling the pressure, velocity, velocity gradient and stress boundary conditions directly. There are two different FEM models commonly in use now.[16] The first one is the mixed method which uses the velocity components and pressure as the dependent variables through a Bubnov–Galerkin formulation. The second one which is used in this paper is the penalty

* For a two-dimensional surface $R_2=\infty$.

function formulation with the principal advantage that the pressure is eliminated from the set of unknown variables by absorbing the continuity equation into the momentum equation.[17] Therefore, the pressure is defined as

$$p=-\lambda\left[\frac{\partial u}{\partial z}+\frac{1}{r^{\beta}}\frac{\partial}{\partial r}(r^{\beta}v)\right], \tag{7}$$

where λ is a large number depending on μ and Re. Substituting for the pressure from equation (7) into the momentum equations (2) and (3), and applying the Galerkin method, the following matrix equations are obtained:

$$\begin{pmatrix}[M] & [0]\\ [0] & [M]\end{pmatrix}\begin{pmatrix}\{\dot{u}\}\\ \{\dot{v}\}\end{pmatrix}+\begin{pmatrix}[C_{11}]+[C_{22}] & [0]\\ [0] & [C_{11}]+[C_{22}]\end{pmatrix}\begin{pmatrix}\{u\}\\ \{v\}\end{pmatrix}$$

$$+\frac{1}{Re}\begin{pmatrix}2[K_{11}]+[K_{22}] & [K_{12}]\\ [K_{12}]^{\mathrm{T}} & [K_{11}]+2[K_{22}]+2\beta[K_{33}]\end{pmatrix}\begin{pmatrix}\{u\}\\ \{v\}\end{pmatrix}$$

$$+\frac{\lambda}{\mu Re}\begin{pmatrix}[L_{11}] & [L_{12}]+\beta[L_{13}]\\ [L_{12}]^{\mathrm{T}}+\beta[L_{13}]^{\mathrm{T}} & [L_{22}]+\beta([L_{23}]+[L_{23}]^{\mathrm{T}}+[L_{33}])\end{pmatrix}\begin{pmatrix}\{u\}\\ \{v\}\end{pmatrix}=\begin{pmatrix}\{R_u\}\\ \{R_v\}\end{pmatrix}, \tag{8}$$

where

$$[M]=\int_{\Omega^e}N_iN_j\,\mathrm{d}\Omega, \tag{9}$$

$$[C_{11}]=\int_{\Omega^e}u_nN_i\frac{\partial N_j}{\partial z}\,\mathrm{d}\Omega,\qquad [C_{22}]=\int_{\Omega^e}v_nN_i\frac{\partial N_j}{\partial r}\,\mathrm{d}\Omega, \tag{10}$$

$$[K_{11}]=\int_{\Omega^e}\frac{\partial N_i}{\partial z}\frac{\partial N_j}{\partial z}\,\mathrm{d}\Omega,\qquad [K_{12}]=\int_{\Omega^e}\frac{\partial N_i}{\partial r}\frac{\partial N_j}{\partial z}\,\mathrm{d}\Omega, \tag{11}$$

$$[K_{22}]=\int_{\Omega^e}\frac{\partial N_i}{\partial r}\frac{\partial N_j}{\partial r}\,\mathrm{d}\Omega,\qquad [K_{33}]=\int_{\Omega^e}\frac{1}{r^2}N_iN_j\,\mathrm{d}\Omega, \tag{12}$$

$$[L_{11}]=\int_{\Omega^e}\frac{\partial N_i}{\partial z}\frac{\partial N_j}{\partial z}\,\mathrm{d}\Omega,\qquad [L_{12}]=\int_{\Omega^e}\frac{\partial N_i}{\partial z}\frac{\partial N_j}{\partial r}\,\mathrm{d}\Omega, \tag{13}$$

$$[L_{22}]=\int_{\Omega^e}\frac{\partial N_i}{\partial r}\frac{\partial N_j}{\partial r}\,\mathrm{d}\Omega,\qquad [L_{13}]=\int_{\Omega^e}\frac{1}{r}\frac{\partial N_i}{\partial z}N_j\,\mathrm{d}\Omega, \tag{14}$$

$$[L_{23}]=\int_{\Omega^e}\frac{1}{r}\frac{\partial N_i}{\partial r}N_j\,\mathrm{d}\Omega,\qquad [L_{33}]=\int_{\Omega^e}\frac{1}{r^2}N_iN_j\,\mathrm{d}\Omega, \tag{15}$$

$$\{R_u\}=\int_{\Gamma}\bar{\tau}_{zz}N_i^*\,\mathrm{d}\Gamma,\qquad \{R_v\}=\int_{\Gamma}\bar{\tau}_{rr}N_i^*\,\mathrm{d}\Gamma, \tag{16}$$

where N_i's are the shape functions for the isoparametric quadrilateral elements in the domain Ω with the boundary Γ. Integrals (9)–(12) and (16) are evaluated by the 2×2 Gauss–Legendre integration rule. The $[L]$ matrices should be singular for the penalty function approach to be successful. A reduced Gauss integration is used to evaluate the $[L]$ matrices given by integrals (13)–(15). The surface traction resulting from the surface tension effects is directly integrable over the free surface using equation (16).

The above formulation is based on the Eulerian or fixed mesh that the location of the nodes does not change with time. In this paper we are going to follow the displacement of the free surface in a Lagrangian sense, which results in the motion of the nodes throughout the mesh. From a physical point of view, this motion of nodes will impose some convective effects on the flow variables. We allow the motion of the nodes in the r direction only according to the following simple rule:

$$z_i(t+\delta t)=z_i(t)=\text{constant}, \qquad r_i(t+\delta t)=cr_i(t), \tag{17}$$

where the subscript i refers to the node number, and $c=c(z, t)$ is a constant for each column of nodes defined as

$$c=\frac{h(z, t+\delta t)}{h(z, t)}. \tag{18}$$

In order to show how this motion affects the convective terms in equations (2) and (3), let us consider the axial velocity u at node i. Denote the time rate of change of this velocity, as appears in equation (2), with $\partial u/\partial t|_{z,r}$. Then for the total change of u in the moving frame of reference, we can write

$$\left.\frac{\partial u}{\partial t}\right|_i=\left.\frac{\partial u}{\partial t}\right|_{z,r}+\left(\frac{\mathrm{d}z}{\mathrm{d}t}\right)_i\left(\frac{\partial u}{\partial z}\right)_i+\left(\frac{\mathrm{d}r}{\mathrm{d}t}\right)_i\left(\frac{\partial u}{\partial r}\right)_i, \tag{19}$$

where the subscript i refers to the derivative in the moving frame of reference. Noting from (17) that $(\mathrm{d}z/\mathrm{d}t)_i=0$, and approximating $(\mathrm{d}r/\mathrm{d}t)_i$ with a backward finite difference in terms of c, we obtain

$$\left.\frac{\partial u}{\partial t}\right|_{z,r}=\left.\frac{\partial u}{\partial t}\right|_i-\frac{c-1}{\delta t}r_i\left(\frac{\partial u}{\partial r}\right)_i. \tag{20}$$

Now, recognizing that $\partial u/\partial t|_{z,r}$ is the same as $\partial u/\partial t$ of equation (2), and dropping the subscripts, we can rewrite equation (2), in the moving co-ordinate, as

$$\frac{\partial u}{\partial t}+u\frac{\partial u}{\partial z}+\left(v-\frac{c-1}{\delta t}r\right)\frac{\partial u}{\partial r}=-\frac{\partial p}{\partial z}+\frac{1}{Re}\left[\frac{\partial^2 u}{\partial z^2}+\frac{1}{r^\beta}\frac{\partial}{\partial r}\left(r^\beta\frac{\partial u}{\partial r}\right)\right]. \tag{21}$$

With a similar argument for the radial momentum equation one can show that

$$\frac{\partial v}{\partial t}+u\frac{\partial v}{\partial z}+\left(v-\frac{c-1}{\delta t}r\right)\frac{\partial v}{\partial r}=-\frac{\partial p}{\partial r}+\frac{1}{Re}\left[\frac{\partial^2 v}{\partial z^2}+\frac{1}{r^\beta}\frac{\partial}{\partial r}\left(r^\beta\frac{\partial v}{\partial r}\right)-\beta\frac{v}{r^2}\right]. \tag{22}$$

These new extra terms will modify the matrix $[C_{22}]$ of the finite element formulation (equation (10)) as

$$[C_{22}]=\int_{\Omega^e}\hat{v}_n N_i\frac{\partial N_j}{\partial r}\mathrm{d}\Omega, \tag{23}$$

where

$$\hat{v}_n=v_n-\frac{c-1}{\delta t}r_i. \tag{24}$$

There is an alternative procedure to obtain the above formulation as adopted by Albert and O'Neill[18] and Keunings.[13] These authors have considered the shape function as a function of time as well as space. By applying the Galerkin method directly on this shape function, they find

the same result as the one shown in (23) and (24). However, we would rather use the procedure explained by (19)–(21) because it is more physically comprehensive.

4. SURFACE ADVECTION

Once the velocities are obtained, the interface has to be advected. In this paper we present a new method for surface advection entitled the Height–Flux Method, abbreviated as HFM. Indeed, HFM is a combination of the height method, which is used with the finite element method, and the flux methods extensively used for surface advection in the finite difference method. The flux method was originally developed by Ashgriz and Poo[6] for 2D Cartesian flows. This method was entitled FLAIR, standing for Flux Line-segment model for Advection and Interface Reconstruction. The FLAIR technique was also implemented for the surface advection based on the velocities obtained from a finite elements solution.[19] This technique is referred to as FEM–VOF and is applicable to very large surface deformations including merging and breaking of liquid regions. However, for the problems that the free surface can be represented by a height function, a much simpler version of the FEM–VOF method can be developed, which is described below.

Consider the domain (2D Cartesian or 3D axisymmetric) shown in Figure 2 which is surrounded by a free surface (shown with the thicker line) at the top. We divide this domain into several vertical subvolumes of width δz_I and volume V_I. The location of the free surface on the left and right sides of this subvolume is given by h_i and h_{i+1} at time t, respectively. Knowing the velocity distributions over the sideplanes, we are going to find the location of the free surface, i.e. h_i and h_{i+1}, at time $t+\delta t$. In order to do this, we first calculate the net flux of the fluid passing through the sideplanes during the time interval δt, and determine the new volume of fluid at the time $t+\delta t$ in the subvolume by adding the net flux to the previous volume at time t. Then we solve the inverse problem to find the new heights, h_i. In the remainder of this section we explain the HFM method for axisymmetric flows; the extension to 2D Cartesian is straightforward.

Figure 2 shows a typical element in the axisymmetric r–z plane along with its isoparametric master element in the ξ–η plane. Since the sideplanes are normal to the axial direction, in flux calculation we need to consider the axial velocity, u, only. Let us consider the side 2–3 of the element e lying on the right sideplane. The flux passing through this side is

$$\delta V_{\mathrm{R}}^{e} = \int_{\Gamma_{23}} u\,\delta t\,\mathrm{d}\Gamma. \tag{25}$$

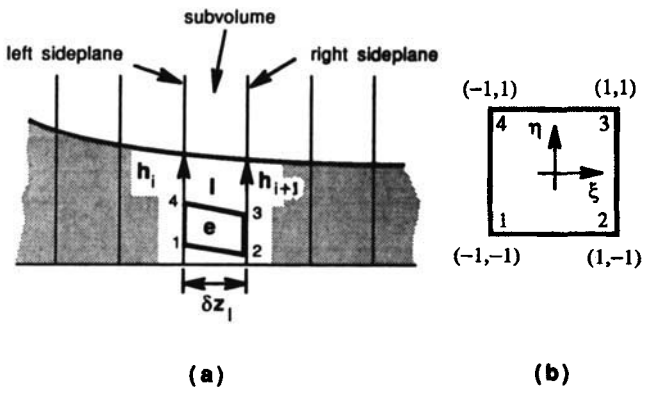

Figure 2. The fluid zone divided into subvolumes represented by their height and thickness (a), and mapping of the Eulerian element, e, into the master isoparametric element (b)

Assuming constant velocity during the time interval δt, we can take δt out of the integral. In the finite element solution, the velocity and radius are approximated by

$$u = u_i N_i \quad \text{and} \quad r = r_i N_i, \tag{26}$$

u_i being the velocity at node i and N_i being the shape function for the isoparametric quadrilateral elements, defined as follows:

$$\begin{aligned} N_1(\xi, \eta) &= \tfrac{1}{4}(\xi - 1)(\eta - 1), \\ N_2(\xi, \eta) &= -\tfrac{1}{4}(\xi + 1)(\eta - 1), \\ N_3(\xi, \eta) &= \tfrac{1}{4}(\xi + 1)(\eta + 1), \\ N_4(\xi, \eta) &= -\tfrac{1}{4}(\xi - 1)(\eta + 1). \end{aligned} \tag{27}$$

Then

$$\delta V_{\mathrm{R}}^e = \delta t \int_{\Gamma_{23}} 2\pi u r \, \mathrm{d}r = 2\pi \, \delta t \int_{\Gamma_{23}} (u_i N_i)(r_j N_j)\left(\frac{\partial r}{\partial \xi}\mathrm{d}\xi + \frac{\partial r}{\partial \eta}\mathrm{d}\eta\right).$$

The side 2–3 of the cell is mapped onto the side 2–3 of the master element where $\xi = 1$ and $\mathrm{d}\xi = 0$. Therefore,

$$\delta V_{\mathrm{R}}^e = 2\pi \, \delta t \int_{-1}^{1} (u_2 N_2 + u_3 N_3)(r_2 N_2 + r_3 N_3)\left(r_2 \frac{\partial N_2}{\partial \eta} + r_3 \frac{\partial N_3}{\partial \eta}\right)\mathrm{d}\eta.$$

After substituting for N_2, N_3 and their derivatives we find that

$$\delta V_{\mathrm{R}}^e = \frac{\pi \, \delta t}{3}(r_3 - r_2)(2r_3 u_3 + r_2 u_3 + r_3 u_2 + 2r_2 u_2). \tag{28}$$

The total flux, δV_{R}, passing through the right sideplane is the summation of δV_{R}^e for all elements in the subvolume. The flux of fluid passing through the left sideplane, δV_{L}, can be calculated in a similar way. Then the new volume of fluid in the subvolume I is

$$V_I(t + \delta t) = V_I(t) + \delta V_{\mathrm{L}} - \delta V_{\mathrm{R}}. \tag{29}$$

To complete the advection process we need to solve the inverse problem of finding the new heights from the new subvolumes. In order to find the height of the interface at the sideplane between every two adjacent subvolumes, V_a and V_b, we assume that the part of the interface which is located in these subvolumes can be approximated by a line segment with the equation

$$h = a\zeta + b, \tag{30}$$

where a and b are two constants yet to be determined. By examining the two adjacent subvolumes, two possibilities for the orientation of the interface line segment, as shown in Figure 3, are realized. First, consider case 1, in which the line segment does not intersect the z axis. Figure 3(a) shows this case with local co-ordinates ζ and h. Knowing the volumes V_a and V_b, the constants a and b of equation (30) are calculated as follows. The fluid volumes in subvolumes a and b are

$$V_a = \frac{\pi \zeta_a}{3}[b^2 + b(a\zeta_a + b) + (a\zeta - a + b)^2],$$

$$V_b = \frac{\pi \zeta_b}{3}\{(a\zeta_a + b)^2 + (a\zeta_a + b)[a(\zeta_a + \zeta_b) + b] + [a(\zeta_a + \zeta_b) + b]^2\}.$$

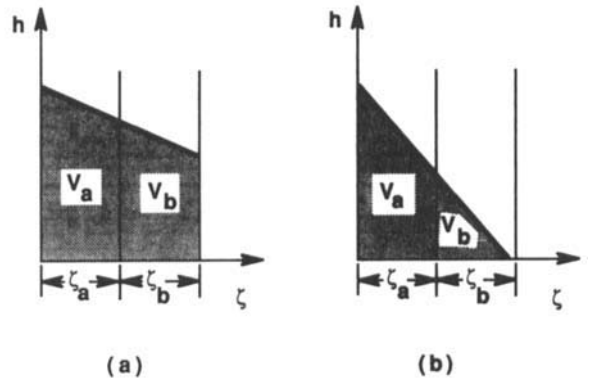

Figure 3. Two different possible cases for free surface representation showing the intersection points of the interface with the subvolume sides

Rearranging,

$$\phi(a, b)=b^2+b(a\zeta_a+b)+(a\zeta_a+b)^2-\frac{3V_a}{\pi\zeta_a}=0,$$
$$\psi(a, b)=(a\zeta_a+b)^2+(a\zeta_a+b)[a(\zeta_a+\zeta_b)+b]+[a(\zeta_a+\zeta_b)+b]^2-\frac{3V_b}{\pi\zeta_a}=0. \tag{31}$$

The above set of two non-linear equations (equation (31)) for a and b is solved numerically using the Newton–Raphson method. Once a and b are found, the height of the common side of the two subvolumes is determined from

$$h=a\zeta_a+b. \tag{32}$$

The analogous set of non-linear equations for case 2, shown in Figure 3(b), is

$$\phi(a, b)=b^2+b(a\zeta_a+b)+(a\zeta_a+b)^2-\frac{3V_a}{\pi\zeta_a}=0,$$
$$\psi(a, b)=(a\zeta_a+b)^3+\frac{3aV_b}{\pi}=0. \tag{33}$$

For any given pair of V_a and V_b, equations (31) are solved first to find a and b, and consequently the heights are obtained at the sideplanes using equation (30). If all the calculated heights are positive, then this pair of subvolumes is case 1, otherwise equations (33), which belong to case 2, are used to calculate the heights.

The accuracy of this surface reconstruction technique is discussed by reconstructing a known surface. First, the volume underneath the known surface is divided into equally spaced subvolumes and the volume enclosed inside each subvolume is calculated. Then, knowing the subvolumes, the surface is reconstructed, and is compared with the known surface. We have considered the axisymmetric surfaces which intersect the r–z plane by the family of curves given as

$$r=r_0+(r_0-0{\cdot}03)\cos 2\pi z. \tag{34}$$

This curve is shown by a solid line in Figure 4 for $r_0=1$. The filled circles indicate the location of the surface found by implementing the HFM reconstruction scheme. N refers to the number of

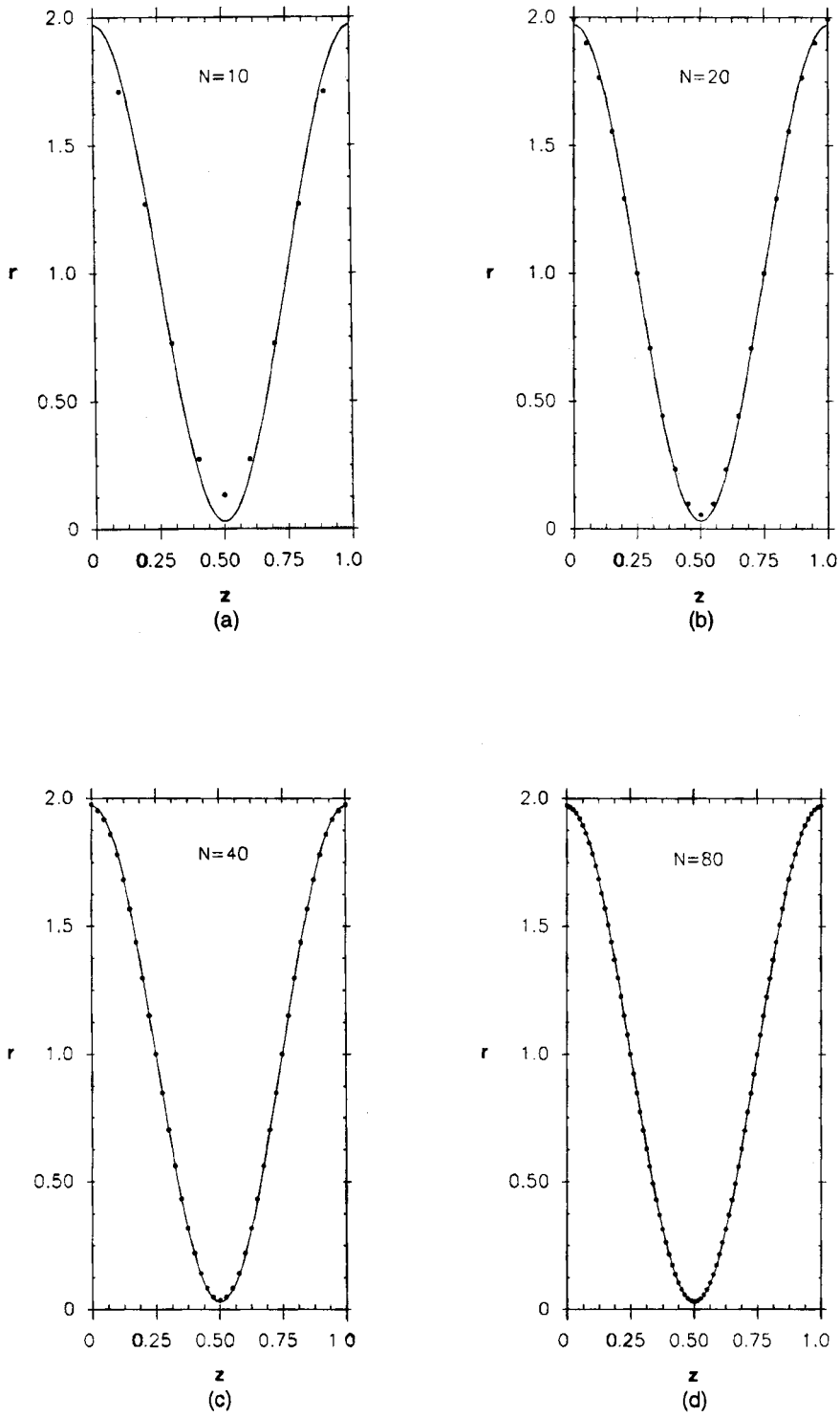

Figure 4. Comparison of the HFM results with the exact solution for a cosine function

subvolumes used for the surface reconstruction. In Figures 4(a)–4(d) we have compared the reconstructed surface with the exact surface for $N = 10, 20, 40$ and 80. As expected, the reconstruction error depends on the curvature of the surface in the r–z plane (i.e. R_1 given in Section 2). Wherever the curvature goes to zero, the error approaches zero as well, because the reconstruction technique is based on the linear approximation of the interface. Therefore, by increasing the number of subvolumes, we are, in fact, improving the reconstructed surface in the regions of higher curvature. Figure 4(c) indicates that with $N = 40$ we can have very good approximation for the surface. Using 80 subvolumes, almost exact reconstruction of the surface is obtained, as seen in Figure 4(d).

By inspecting Figures 4(a)–4(d) it is concluded that the maximum reconstruction error always happens at the minimum point of the curve, i.e. $z = 0{\cdot}5$. Figure 5 gives the number of divisions (subvolumes) required to keep the error at $z = 0{\cdot}5$ less than 0·005, as a function of the curvature at this point. The curvature has been varied by changing r_0 in equation (34), while the other parameters were kept constant. The number of divisions has to be an even integer; therefore, the curvature is not varied continuously and the curve shown in Figure 5 is not smooth. Figure 5 shows that the higher the curvature, the more divisions are needed to keep the error less than some particular value (0·005 in this case).

Variation of the reconstruction error at $z = 0{\cdot}5$, as a function of curvature for $N = 40$ is shown in Figure 6. Increasing the curvature enhances the error almost linearly. Knowing the variation of the curvature along a particular surface, Figure 6 gives an estimation of the expected error at different points of the surface. For instance, consider the free surface shown in Figure 7. (This is the half-wavelength of an infinitely long water jet which is discussed in Section 5). In Figure 8 the curvature at different points of this surface is given for $N = 40$. The absolute value of maximum curvature of this surface is seen to be less than 2·5. Therefore, from Figure 6 the maximum reconstruction error is approximated to be less than 0·0005.

To summarize the sequence of operations involved in HFM, consider Figure 9. Due to the symmetry, only the half-wavelength of the jet is considered. The initial fluid domain is seen in

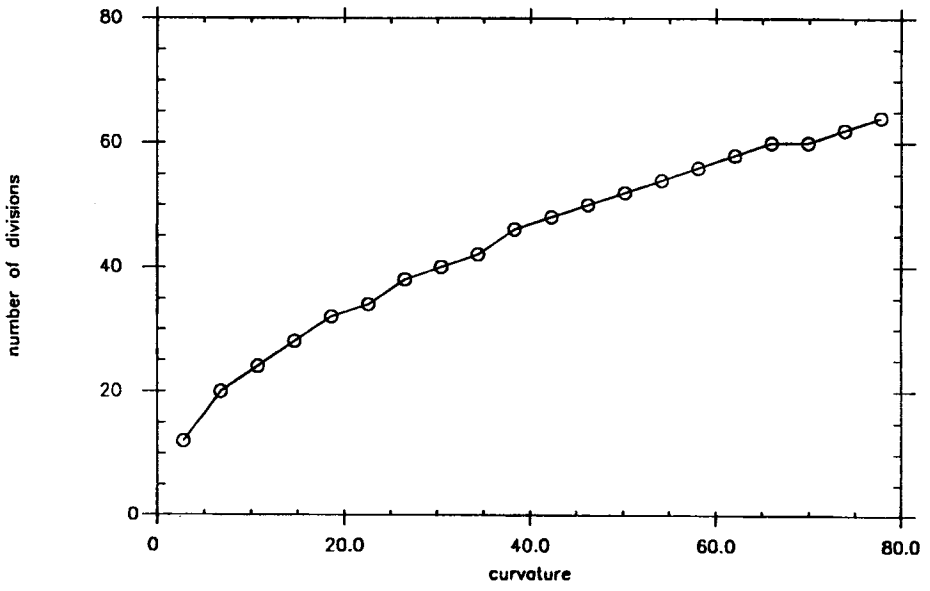

Figure 5. Number of divisions, N, needed to keep the calculated error of curvature at $z = 0{\cdot}5$ of Figure 4 to less than 0·005

Figure 9(a), where the free surface is indicated at the top by the thicker line. The domain is discretized by ten subvolumes, with the amount of fluid in each subvolume as shown in Figure 9(b). Then, this set of numbers is transformed to the free surface, implementing the method described in this section. The finite element mesh generated based on this free surface is depicted in Figure 9(c). When the flow equations are solved, the velocity field is found as shown by the velocity vectors in Figure 9(d). The new subvolumes are obtained using equation (29). The numbers corresponding to these new subvolumes are shown in Figure 9(e). In the final step, the new free surface is reconstructed based on these numbers, and the new finite element mesh is generated as depicted in Figure 9(f). This completes the sequence of the operations needed in the first time step. In continuation, the steps shown in Figures 9(d)–9(f) are repeated.

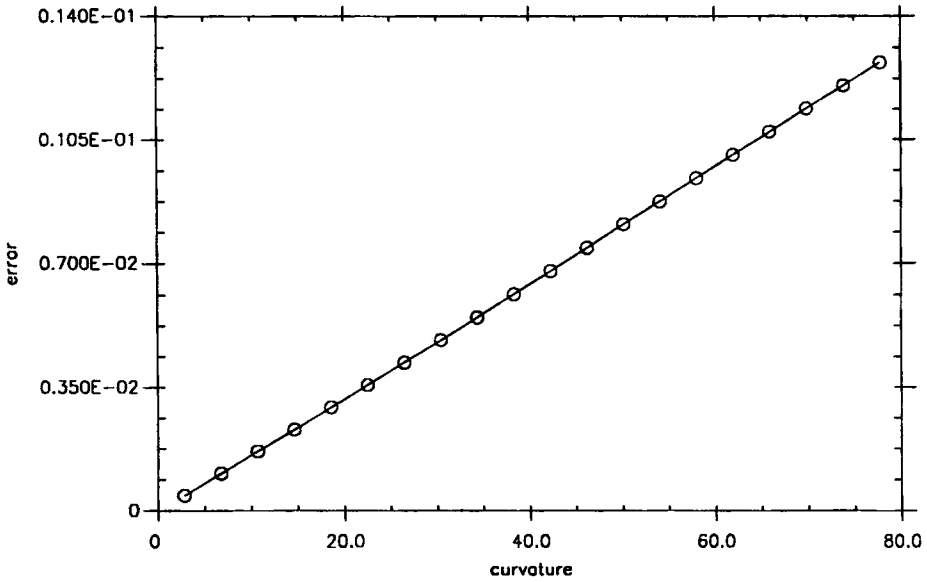

Figure 6. The calculated error for the curvature at $z=0{\cdot}5$ of Figure 4 for $N=40$

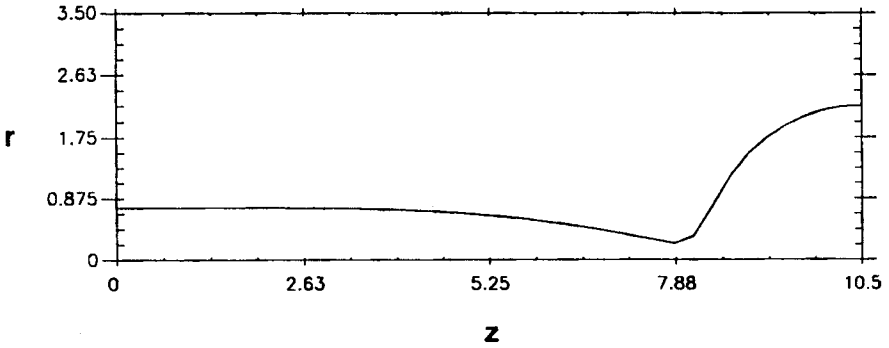

Figure 7. Surface shape of an unstable liquid jet (half-wavelength)

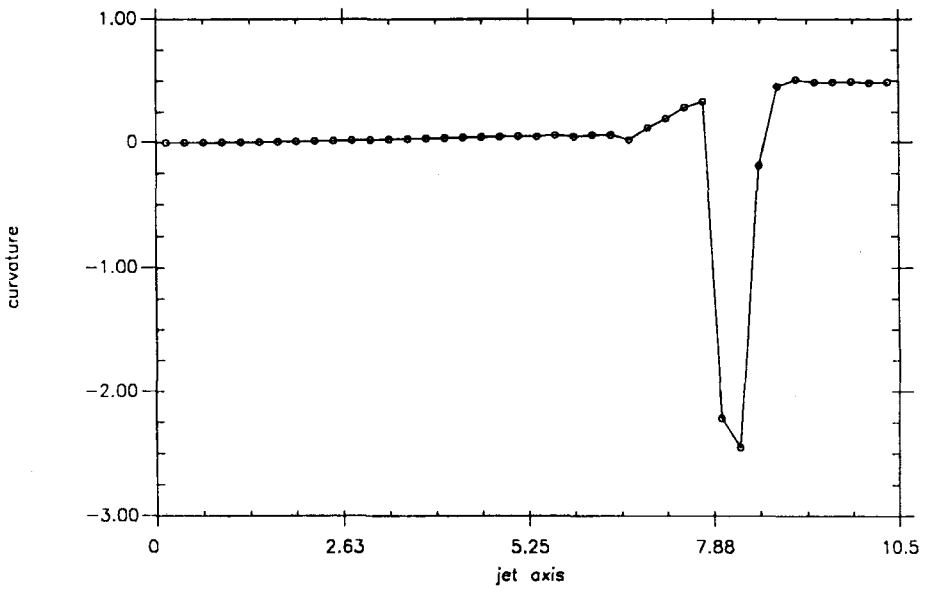

Figure 8. Curvature at various locations of the surface presented in Figure 7

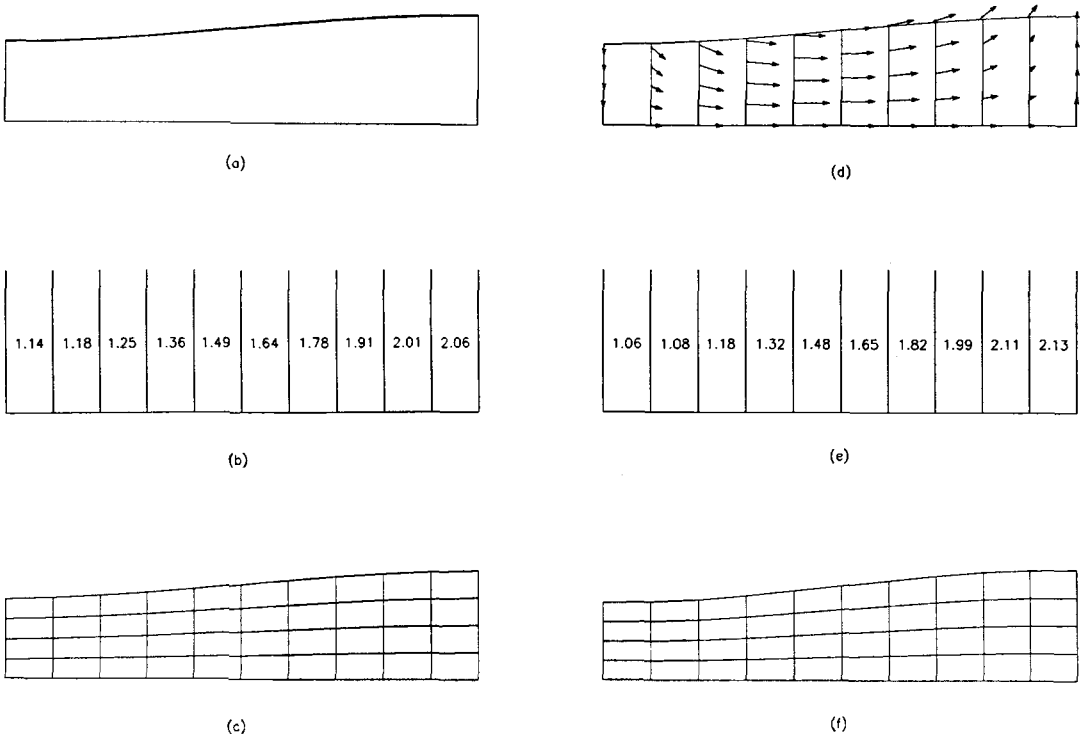

Figure 9. Illustration of the steps taken in HFM: (a) definition of the initial surface shape; (b) subdivision of the domain into subvolumes and description of the subvolume quantity; (c) mesh generation; (d) calculation of the velocity field; (e) advection of the liquid and calculation of the new subvolume quantities; (f) reconstruction of the new surface and mesh system

5. TEMPORAL INSTABILITY OF LIQUID JETS

The HFM is implemented to simulate the breakup of capillary jets. This problem is chosen to test HFM since numerous experimental, analytical and numerical information is available to compare our results with. The linear solution for the instability of inviscid jets is given by Rayleigh[20] and of viscous jets by Chandrasekhar.[21] The linear analysis could not predict the experimentally observed satellite drops. Non-linear instability of inviscid capillary jets has been studied by several investigators, such as Yuen;[22] however, the non-linear instability of viscous jets has not been the subject of analytical investigations. The experimental and numerical studies cover a broader range and are reported by a large number of researchers such as Goedde and Yuen[23] and Vassallo and Ashgriz,[24] and numerically by Bousfield *et al.*[14] and Mansour and Lundgren.[25]

We have considered the breakup of infinitely long jets in vacuum, subject to an initially periodic surface disturbance of the form

$$r(z)=1+\eta_0\cos(kz),$$

where η_0 and k are the amplitude and the wave number, respectively. It is assumed that the jet velocity is much larger than the characteristic capillary speed and a temporal study is appropriate. Therefore, only one wavelength of the jet is considered and symmetric boundary conditions are applied. The undisturbed radius of the jet is selected as the length scale, and the time scale is obtained by equating the Weber number to some constant.

First, we will consider the breakup of a water jet with $Re=331{\cdot}2$, $k=0{\cdot}3$ and the initial amplitude $\eta_0=0{\cdot}001$. This problem has been studied by Mansour and Lundgren[25] using a highly accurate boundary integral method, assuming inviscid fluid. We put $We=2$ for this problem in order to obtain the same velocity scale as the one employed by Mansour and Lundgren.[25] We

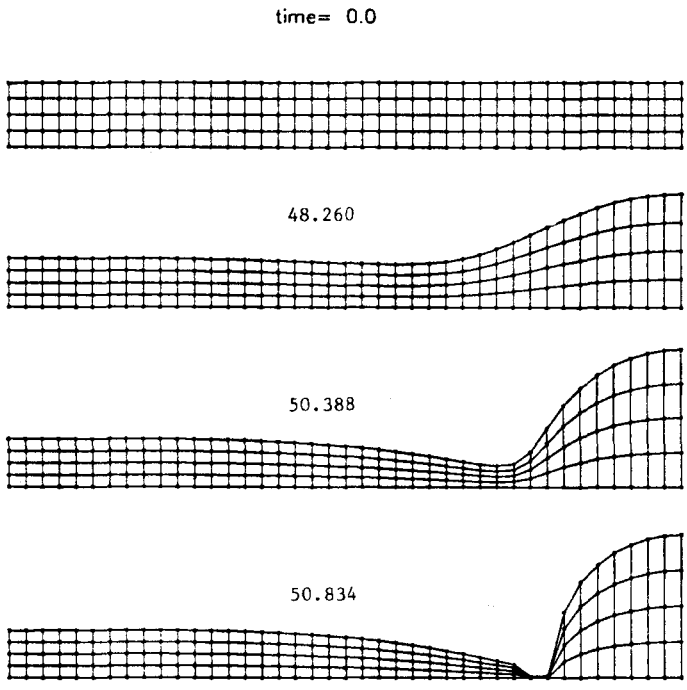

Figure 10. Evolution of the FEM mesh system for the liquid jet instability

have solved this problem with a relatively coarse mesh—40 × 4 linear quadrilateral elements. The initial finite element mesh at time $t=0$ along with the deformed mesh at three other times, including the breakup time $t_b=50{\cdot}834$, are seen in Figure 10. Due to the effects of the surface tension, fluid is pushed from the region with smaller radius towards the higher-radius regions of the jet and the location of the point with minimum radius will change. Eventually, the jet breaks into main and satellite drops. The breakup time is in excellent agreement with the breakup time obtained by Mansour and Lundgren,[25] i.e. $t_b=50{\cdot}9$.

The growth rate of the interface disturbances is calculated following the procedure described by Donnelly and Glaberson.[26] The exponential growth rate, ω, is defined by $\eta=\eta_0 e^{\omega t}$. Then

$$\omega=\frac{1}{t}\ln\left(\frac{\eta}{\eta_0}\right).$$

Therefore, ω is the slope of the curve $\ln(\eta/\eta_0)$ versus time when the curve is approximated by a line. Figure 11 shows the variation of the logarithmic amplitude versus time for swell, neck, and the difference between them. Note that the swell and neck are defined as the locations on the jet axis corresponding to the maximum and minimum jet radius at the initial time, respectively, and their positions are fixed in time. The exponential growth rate is not a constant at different points of the jet surface. However, as suggested by Yuen,[22] and also observed in Figure 11, the exponential growth rate of the difference between swell and neck may be considered constant up to a high degree of accuracy. The growth rate obtained by this method is $\omega=0{\cdot}195$, which compares very well with the analytical result of Chandrasekhar,[21] $\omega=0{\cdot}200$, for the same jet. It is also in good agreement with the experimental results of Goedde and Yuen.[23]

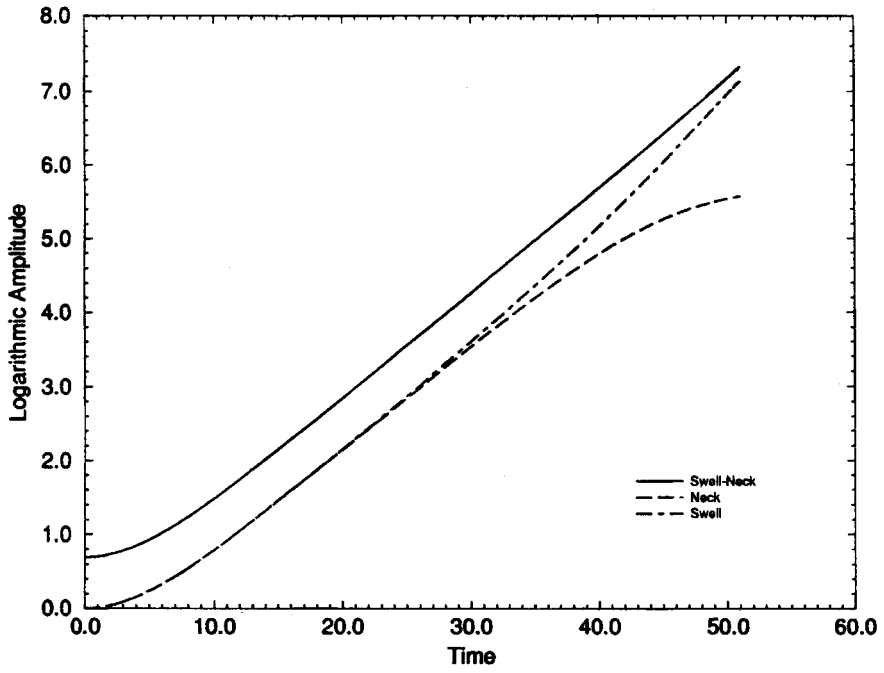

Figure 11. Variation of the amplitude of the swell, neck and the difference between them as a function of time for a jet with $Re=331{\cdot}2$, $We=2$ and $k=0{\cdot}3001$ with $\eta_0=0{\cdot}001$

We have compared the HFM and the original height method where the evolution of the free surface is calculated by the kinematic condition for the surface:

$$\frac{\partial h}{\partial t}+v_s\frac{\partial h}{\partial x}=u_s,$$

where u_s and v_s are the velocity components at the free surface and h is the height function. The

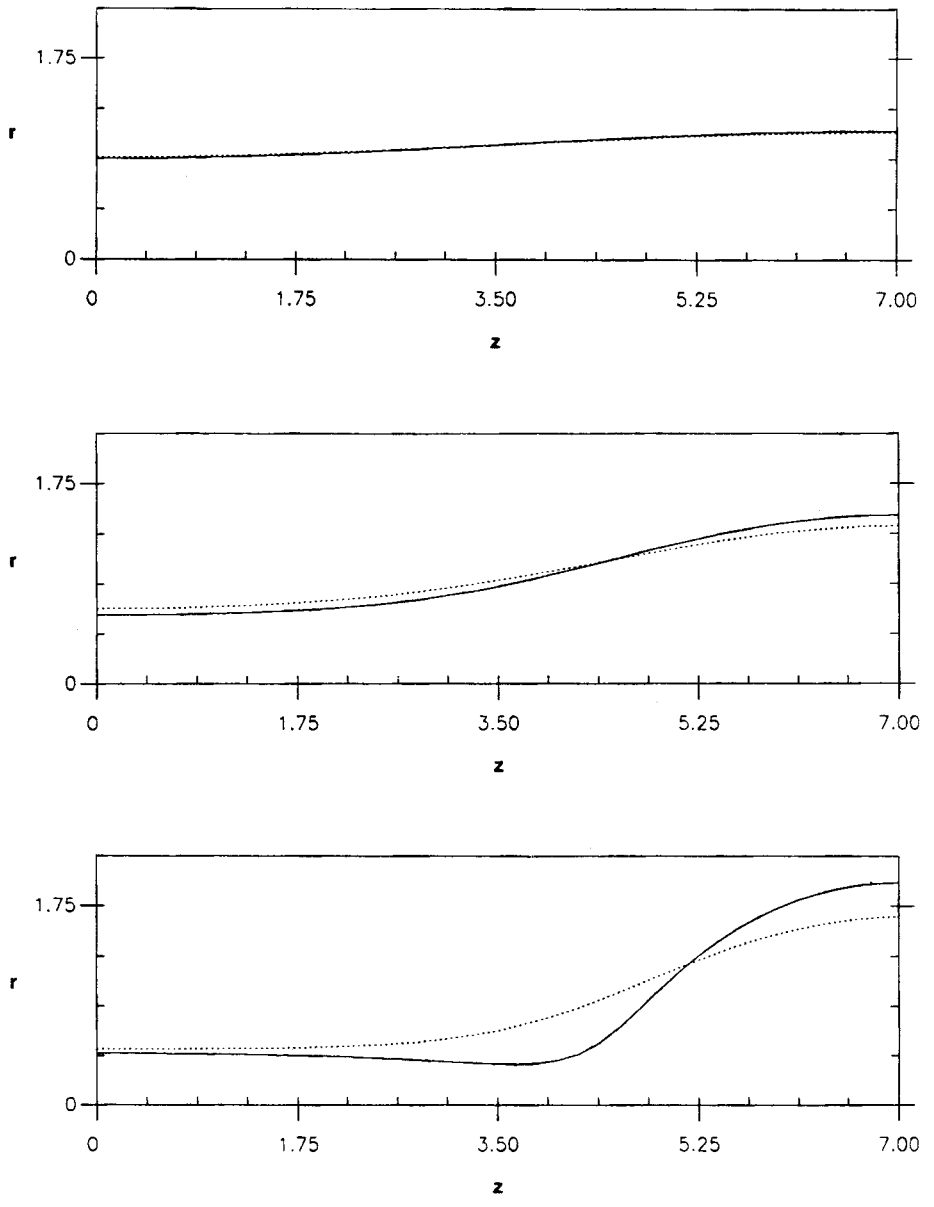

Figure 12. Comparison of the calculated jet surface evolution by the HFM (—) and the height method (· · ·) for a jet with $Re=10$, $We=1$, $k=0{\cdot}4488$ and $\eta_0=0{\cdot}05$

same number of linear quadrilateral elements (160) and the same time step are used in both calculations. Also, the initial disturbance is the same in both cases. Figure 12 shows large differences between the results of the two techniques for a jet with $Re=10$, $We=1$, $k=0{\cdot}4488$ and $\eta_0=0{\cdot}05$. The height method cannot follow the actual surface motion at this grid resolution. Only after the grid resolution is increased and the time step reduced, the height method produces accurate results, as shown by Keunings.[13] Therefore, the HFM is a more efficient technique for the study of free surface flows where extensive parametric studies are needed.

A detailed investigation of the breakup of a water jet ($Re=200$, $We=1$ and $\eta_0=0{\cdot}05$) for various disturbance wave numbers is completed. Figure 13 shows the influence of the wave number on the sizes of the main and satellite drops. The increase in the wave number is shown to result in the formation of shorter and thinner liquid ligaments, and consequently smaller satellite drops. The theoretically predicted values are compared with the experimentally measured drop sizes obtained by Lafrance[27] and Rutland and Jameson.[28] The calculated results are in excellent agreement with the experimental data.

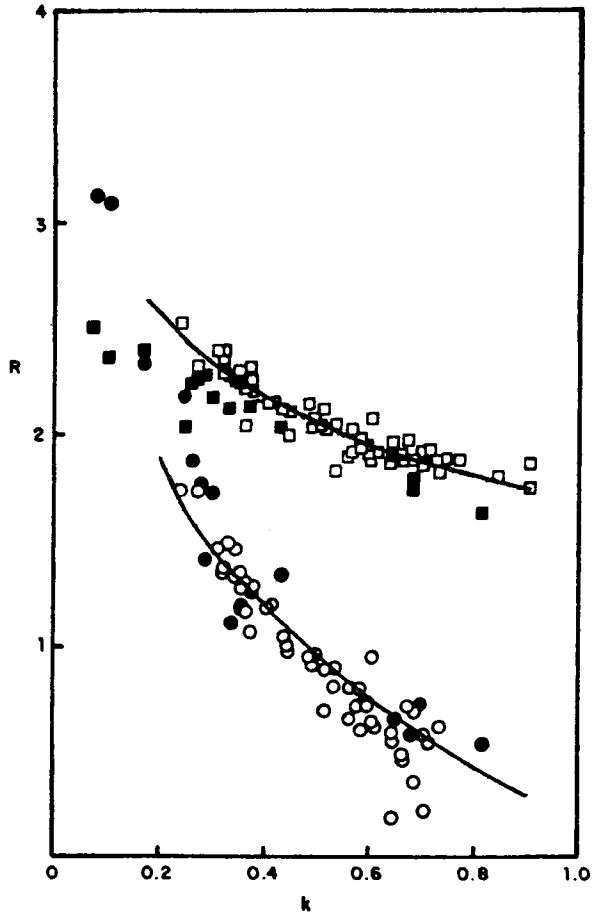

Figure 13. Predicted (solid line) and measured (symbols) values of the main and satellite drop sizes for a water jet ($Re=200$, $We=1$ and $\eta_0=0{\cdot}05$) at various disturbance wave numbers

The effect of Re on the growth rate of the disturbances and the sizes of the drops is also considered. Figure 14 shows the breakup of a capillary jet with $Re=10$, $We=1$, a disturbance wave number $k=0{\cdot}4488$ and amplitude $\eta_0=0{\cdot}05$. The same number of elements as in the previous problem has been used, i.e. 160 linear quadrilateral elements. The breakup time for the low-Re jet of Figure 14 has increased to $t_b=14{\cdot}269$. Also, comparison with Figure 10 reveals that lowering the Re will result in thinner ligament and larger main drops. Figure 15 depicts the variation of logarithmic amplitude with time for this jet. These results clearly show the deviation of the growth rate from the linear theory.

The effect of the wave number on the low-Re jet is considered next. Figure 16 shows the history of the surface deformation for a jet with $Re=10$, $We=1$, $k=0{\cdot}6283$ and $\eta_0=0{\cdot}05$, with a finite element mesh consisting of 80 linear elements. Again, the results show a reduction in the satellite size with an increase in the wave number. The variation of logarithmic amplitude of the swell, neck, and the difference between them with time are presented in Figure 17. Comparing Figure 17 with Figure 15 shows that at lower wavelengths the growth rates behave more linearly. It can be clearly seen that the logarithmic amplitude curves of Figure 17 stay parallel to each other and almost linear for most of the time before the breakup. To verify the accuracy of the results, we have repeated the problem using a refined mesh with 160 elements. Table I compares the results at the breakup time and indicates that they are in very good agreement. All the parameters used for this jet are the same as those shown in Figure 14, except for the wave number, which is increased by 40%.

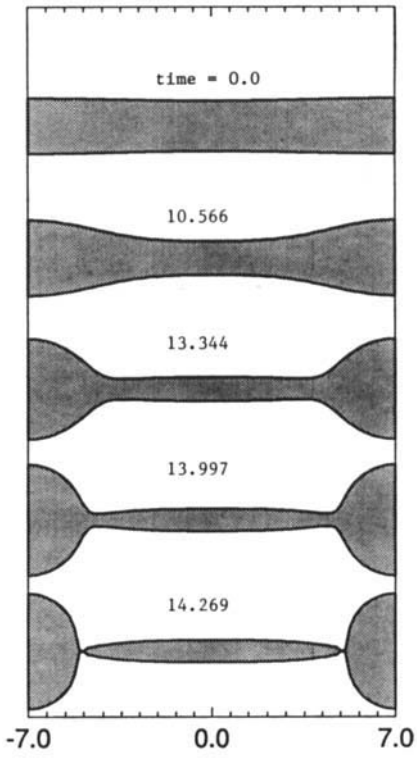

Figure 14. The time-resolved simulation of the breakup of a liquid jet: $Re=10$, $We=1$ and disturbance wave number $k=0{\cdot}4488$ with $\eta_0=0{\cdot}05$

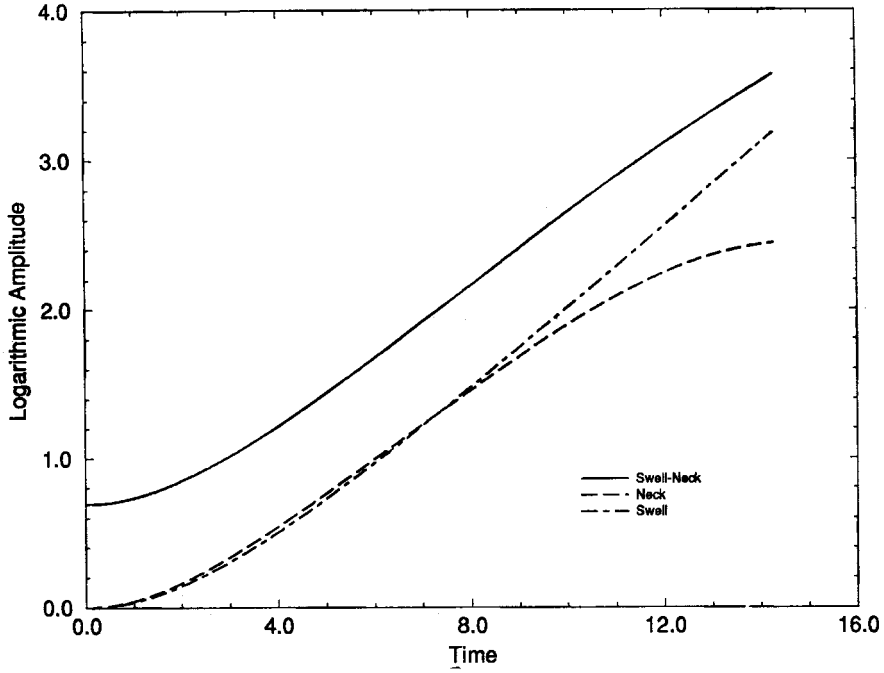

Figure 15. Variation of the amplitude of the swell, neck and the difference between them as a function of time for a jet with $Re=10$, $We=1$ and $k=0{\cdot}4488$ with $\eta_0=0{\cdot}05$

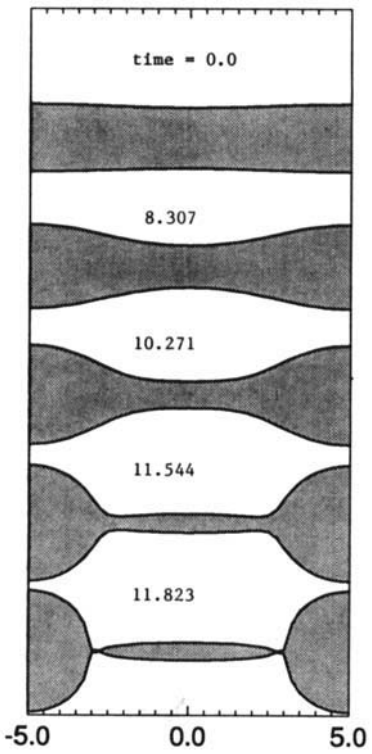

Figure 16. The time-resolved simulation of the breakup of a liquid jet: $Re=10$, $We=1$ and disturbance wave number $k=0{\cdot}6283$ with $\eta_0=0{\cdot}05$

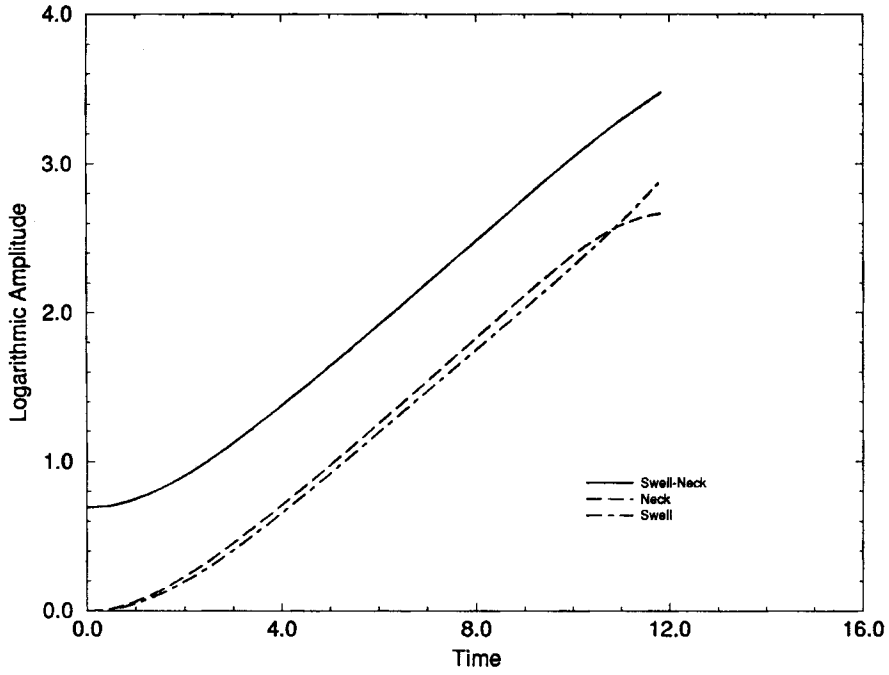

Figure 17. Variation of the amplitude of the swell, neck and the difference between them as a function of time for a jet with $Re=10$, $We=1$ and $k=0{\cdot}6283$ with $\eta_0=0{\cdot}05$

Table I. The effect of mesh refinement on the accuracy of the results.

	Breakup time	Breakup point	Neck radius	Swell radius
Coarse mesh (20 × 4)	11·823	2·750	0·2801	1·8982
Fine mesh (40 × 4)	11·852	2·875	0·2785	1·9126

6. CONCLUSION AND COMMENTS

A new method is developed for the study of free surface flows using the finite element method with penalty formulation, and a flux method for surface advection. The advection part is completely independent of the momentum solver; however, it can easily be combined with any finite element code. The accuracy and efficiency of this technique is shown through the study of capillary breakup of liquid jets. The results indicate that the satellite drop size reduces with increasing wave number. The theoretically calculated main and satellite drop sizes were in excellent agreement with the experimentally measured values. Numerical experiments indicate the ability of the method in handling large surface deformations and its accuracy using a coarse mesh and large time steps. Therefore, this method can be implemented to perform extensive studies of free surface flows. Further extension of this technique is possible to include the energy equation. The spatial study of the instability of jets is also feasible through the improvement of the method to allow generation of new subvolumes.

REFERENCES

1. F. H. Harlow and J. F. Welch, 'Numerical calculation of time-dependent viscous incompressible flow of fluid with free surface', *Phys. Fluids*, **8,** 2182 (1965).
2. W. F. Noh and P. Woodward, 'SLIC (simple line interface calculation)', in A. I. van de Vooren and P. J. Zandbergen (eds), *Proc. 5th Int. Conf. on Numerical Methods in Fluid Dynamics*, Lecture Notes in Physics, Vol. 59, Springer, New York, 1976, pp. 330–340.
3. B. D. Nichols, C. W. Hirt and R. S. Hotchkiss, 'SOLA-VOF: a solution algorithm for transient fluid flow with multiple free boundaries', *Los Alamos Scientific Lab. Report No. LA8355*, 1980.
4. C. W. Hirt and B. D. Nichols, 'Volume of fluid (VOF) method for the dynamics of free boundaries', *J. Comput. Phys.*, **39,** 201 (1981).
5. H. Miyata and S. Nishimura, 'Finite-difference simulation of nonlinear ship waves', *J. Fluid Mech.*, **157,** 327 (1985).
6. N. Ashgriz and J. Y. Poo, 'FLAIR: flux line-segment model for advection and interface reconstruction', *J. Comput. Phys.*, **93,** 449 (1991).
7. R. Bonnerot and P. Jamet, 'Numerical computation of the free boundary for the two-dimensional Stefan problem by space–time finite elements', *J. Comput. Phys.*, **25,** 163 (1977).
8. H. Saito and L. E. Scriven, 'Study of coating flow by the finite element method', *J. Comput. Phys.*, **42,** 53 (1981).
9. C. S. Frederiksen and A. M. Watts, 'Finite-element method for time-dependent incompressible free surface flow', *J. Comput. Phys.*, **39,** 282 (1981).
10. D. R. Lynch, 'Unified approach to simulation on deforming elements with application to phase change problems', *J. Comput. Phys.*, **47,** 387 (1982).
11. H. Ettouney and R. A. Brown, 'Finite element method for steady solidification problems', *J. Comput. Phys.*, **49,** 118 (1983).
12. M. S. Engelman and R. L. Sani, 'Finite element simulation of incompressible fluid flows with a free/moving surface', *Recent Advances Numer. Methods Fluids*, **5,** 47 (1986).
13. R. Keunings, 'An algorithm for the simulation of transient viscoelastic flows with free surfaces', *J. Comput. Phys.*, **62,** 199 (1986).
14. D. W. Bousfield, R. Keunings, G. Marrucci and M. M. Denn, 'Nonlinear analysis of the surface tension driven breakup of viscoelastic filaments', *J. Non-Newt. Fluid Mech.*, **21,** 79 (1986).
15. S. F. Kistler and L. E. Scriven, 'Coating flows', in J. R. A. Pearson and S. M. Richardson (eds), *Computational Analysis of Polymer Processing*, Applied Science Publishers, New York, 1983, p. 243.
16. K. H. Huebner, *The Finite Element Method for Engineers*, Wiley, New York, 1982.
17. T. J. R. Hughes, W. K. Liu and A. Brooks, 'Finite element analysis of incompressible viscous flows by the penalty function formulation', *J. Comput. Phys.*, **30,** 1–60 (1979).
18. M. R. Albert and K. O'Neill, 'Moving boundary moving mesh analysis of phase change using finite elements with transfinite mappings', *Int. j. numer. methods eng.*, **23,** 591–607 (1986).
19. F. Mashayek and N. Ashgriz, 'A hybrid finite element–volume of fluid method for simulating liquid atomization', in *6th Ann. Conf. on Liquid Atomization and Spray Systems*, Worcester, MA, 17–19 May 1993.
20. W. S. Rayleigh, 'On the instability of jets', *Proc. Lond. Math. Soc.*, **10,** 4–13 (1879).
21. S. Chandrasekhar, *Hydrodynamic and Hydromagnetic Stability*, Clarendon, Oxford, 1961.
22. M. C. Yuen, 'Non-linear capillary instability of a liquid jet', *J. Fluid Mech.*, **33,** 151–163 (1968).
23. E. F. Goedde and M. C. Yuen, 'Experiments on liquid jet instability', *J. Fluid Mech.*, **40,** 495–511 (1970).
24. P. Vassallo and N. Ashgriz, 'Satellite formation and merging in liquid jet breakup', *Proc. Roy. Soc. Lond.*, **A433,** 269–286 (1991).
25. N. N. Mansour and T. S. Lundgren, 'Satellite formation in capillary jet breakup', *Phys. Fluids*, **A2,** 1141–1144 (1990).
26. R. J. Donnelly and W. Glaberson, 'Experiment on capillary instability of a liquid jet', *Proc. Roy. Soc. Lond.*, **A290,** 547–556 (1966).
27. P. Lafrance, 'Non-linear breakup of a laminar liquid jet', *Phys. Fluids*, **18,** 428 (1975).
28. D. F. Rutland and G. J. Jameson, 'Theoretical prediction of the sizes of drops formed in the breakup of capillary jets', *Chem. Eng. Sci.*, **25,** 1689 (1970).